2024 IEEE/RSJ International Conference on Intelligent Robots and Systems (IROS)
October 14-18, 2024. Abu Dhabi, UAE

# Vine Robots that Evert through Bending

Rui Wu[1,2] and Stefano Mintchev[1,2]

***Abstract*— Despite the elegantly simple operation principle, the design of everting vine robots still presents two complexities: a tip-device required for buckle-free retraction; a pressurised base chamber to maintain inflation while allowing the everted body to be winded onto a motorised reel. We create a new type of vine robots with a unique eversion method: instead of using a single everting tube, our design comprises multiple interconnected tubes that bend to induce an overall eversion. Our design eliminates the pressurised base and the tip-device, while allowing buckle-free retraction. It also enables new designs and functionalities beyond conventional vine robots, including drone-based vine robots capable of cantilevered operations, everting grippers that grasp then transport objects into the robot body, and solid-state vine robots without the need for inflation.**

## I. INTRODUCTION

As a category of soft robots, everting vine robots have an unique deployment capability that allows the robot to transform from a compact storage state into a extended, slender tubular structure [1], [2]. This capability opens new avenues in various applications such as search and rescue [1], [3], inspection [4], [5], [6], [7], surgery catheters [8], [9], deployable manipulators or actuators [10], [11], [12], ground-burrowing [13], [14], [15], and deployable devices that grow into designable shapes [16], [17], [18], [19]. The remarkable versatility and adaptability underscore the robot's innovative potential across diverse fields.

However, challenges persist in retracting the tubular body, which is prone to longitudinal buckling under retraction forces [20], as depicted in Figure 1. Retraction of vine robots is enabled by eversion of the tubular body, which is resisted by the internal pressure, leading to high retraction forces that cause buckling of its slender body. Additionally, the less-constrained, everted material (i.e., the tail) often shifts away from the tube's central axis, creating a bending moment that further destabilises the body. Although a shorter robot is in theory more stable, according to simple analysis in Section II-B, the tail's lateral shift alone can lead to a zero retractable length, thus a robot with any length can become non-retractable when its tail is off-centered due to gravity or the robot's initial curvature. As a result, most vine robots are designed for non-retractive applications [18], [19], [21], or for applications that allow the robot to gain stability through external contact with the environment during retraction [13], [22], [23], [24].

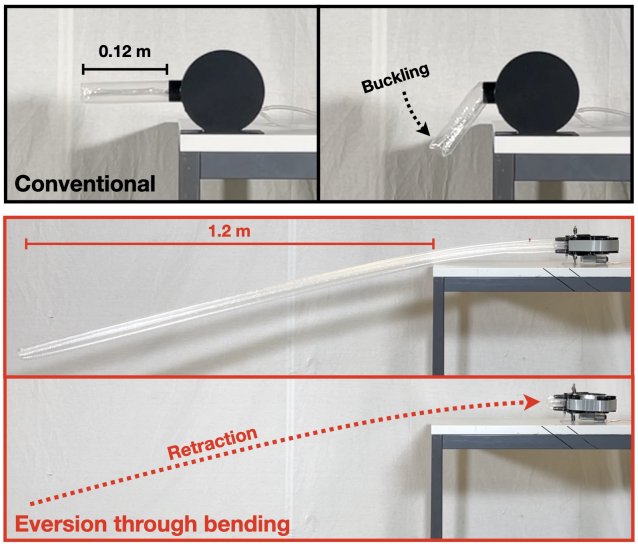


Fig. 1. Eversion through bending allows buckle-free retraction of a cantilevered robot, while eliminating the pressurised base chamber, as demonstrated by the comparison between a conventional vine robot with simple tube eversion (top), and our design with bending-eversion (bottom)

In existing studies, buckling-free retraction is usually achieved by tip-located retraction devices, which apply the retraction force directly on the tip, localizing the destabilising load and preventing buckling [20]. These devices may employ motorised mechanisms [20], [22] or soft pneumatic actuators [23]. However, they introduce additional weight and complexity, and in demanding scenarios, such as retraction from a cantilevered position, buckling-free retraction remains a challenge since the cantilever distance is severely limited by the weight of tip-devices. Another recent study has demonstrated buckling-free retraction of vine robots utilising hyperelastic tube material that shrinks from the tip during retraction [25]. However, although the shrinking tip reduces retraction force thus helps stabilising the robot, the tail's off-center shift is still not constrained.

To enable both deployment and retraction under the most demanding, cantilevered scenario, we revisit the basic principle of eversion, and introduce a new type of vine robot composed of multiple tubes that evert through bending (Figure 1). This bending-induced eversion significantly reduces the retraction force, as it is not resisted by the inflation pressure, and the everted tubes remain inflated thus aligned with the central axis, ensuring stability. As a result, the

*This work was supported by the Swiss National Science Foundation through the Eccellenza Grant (proposal number 186865), by the Horizon Europe project SPEAR (proposal number 101119774) with the contribution of State Secretariat for Education, Research and Innovation (SBFI No. 23.00316)

[1]Environmental Robotics Laboratory, Department of Environmental Systems Science, ETH Zurich, 8092 Zurich, Switzerland

[2]Swiss Federal Institute for Forest, Snow and Landscape Research (WSL), 8903 Birmensdorf, Switzerland. rui.wu@usys.ethz.ch

robot enables buckling-free retraction from a cantilevered position with a cantilevered length of over 1 m, while eliminating the need for a tip-device (Figure 1), which is not possible with previous designs. In addition, our design also removes the pressurised root chamber in conventional vine robots, since the retraction mechanisms can be installed outside the pressurised region. This paper will discuss the design, analyses, fabrication, and experimental validation of our design. We also demonstrate some capabilities beyond conventional everting robots in Section IV, demonstrating an eversion-based robotic gripper, a cantilevered vine robot installed on a drone platform, and a solid-state vine robot made of flexible foam that do not require inflation.

## II. EVERSION THROUGH BENDING

In this section, we present the basic principle, analyses and experimental validation of the retraction and deployment enabled by bending-eversion.

### A. Working Principle

Conventional vine robots typically retract by drawing the tail, i.e., the everted tube, into the tubular body, as illustrated in Figure 2A. The high buckling tendency is primarily caused by two effects: 1) the significant retraction force needed to counteract the pressure force, creating substantial axial compression between the tip and the root; 2) a tendency for the tail to deviate from the central axis, introducing a bending moment that compromises the robot's stability.

We propose a new vine robot design as depicted in Figure 2B. Our robot consists of three main components: soft everting body, retraction mechanism, and inflation system, which is further detailed in Section III. The retraction mechanism uses a motorised reel with a mechanical compressor to deflate and retrieve the tubes onto a mandrel. The inflation system maintains a prescribed air pressure during operations.

Instead of a single self-everting tube, our design comprises multiple, or in this case three inflated tubes that are bonded together through a connective tube (the red tube in the figure). During deployment or retraction, the connective tube everts similarly to a conventional vine robot, and the three inflated tubes evert through bending.

During this bending-induced eversion, the location of the bending point moves along the tubes while the bending angles remain 180°, making the process isovolumetric, thus the eversion is not resisted by internal pressure. As a result, the retraction force is substantially reduced, addressing a primary cause of buckling in conventional designs. The isovolumetric eversion also enables vine robot made of non-inflated solid-state materials such as foam, as discussed in Section IV

After eversion, the tail stays inflated and constrained to the central axis by the connective tube, resembling a Bowden cable that transmits compressive load despite its slender form (considering the tail as equivalent to the inner wire, and the outer body as the flexible cable housing) [26]. This removes the other primary cause of buckling discussed above. The robot is therefore retractable without using a tip-located retraction device, and as discussed later, retraction can be conduced under an cantilevered position.

### B. Retractability Analysis

Retraction of conventional vine robots is analysed according to Figure 2C, where we consider the tube rotating counterclockwise around point $O$ during buckling scenarios. To achieve buckle-free retraction, the following condition must be met, involving the restoring moment caused by inflation pressure $M_{restore}$, the bending moment due to retraction $M_{retract}$, and any external moment $M_{ex}$ (e.g., from gravity in a cantilevered setup), all evaluated with respect to point $O$:

$$M_{restore} \geq M_{retract} + M_{ex} \tag{1}$$

where

$$M_{restore} = P \cdot A \cdot R \tag{2}$$

$$M_{retract} = T(R+d) \tag{3}$$

here $A$ and $R$ represent the cross-sectional area and radius of the robot, $P$ is the inflation pressure, and $d$ signifies the tail's lateral shift from the central line, possible friction on the tail is neglected. The retraction force $T$ is calculated as:

$$T = \frac{1}{2} P \cdot A + F_I \tag{4}$$

where the factor of $\frac{1}{2}$ accounts for the fact that the tip travels at half the speed of the tail. $F_I$ is an everting force arising from the tube material's resistance to eversion, typically in the order of 1 N and considerably lower than the pressure force [20]. The equations above give the condition for the buckle-free retraction of a conventional vine robot under an external moment:

$$\frac{1}{2} P \cdot A(R-d) \geq F_I(R+d) + M_{ex} \tag{5}$$

It is evident that as the tail offset $d$ approaches $R$, buckling-free retraction becomes unfeasible for a conventional vine robot, even without any external moment $M_{ex}$. In reality, such a tail offset is often inevitable due to curvature caused by initial defect or external load on the robot.

In our design, the retraction force $T$ as experienced by the tail is given by:

$$T = F_I + f \tag{6}$$

where $F_I$ is the tube material's resistance to eversion, and $f$ is the friction force between the tail and the outer tubes. Note that $T$ is independent of $P$ since the eversion is not resisted by pressure, as discussed in Section II-A.

The tail's lateral shift $d$ becomes zero since the tail remains inflated after eversion, and is constrained by the connective tube. The bending moment due to retraction therefore becomes:

$$M_{retract} = T(R - R_t) \tag{7}$$

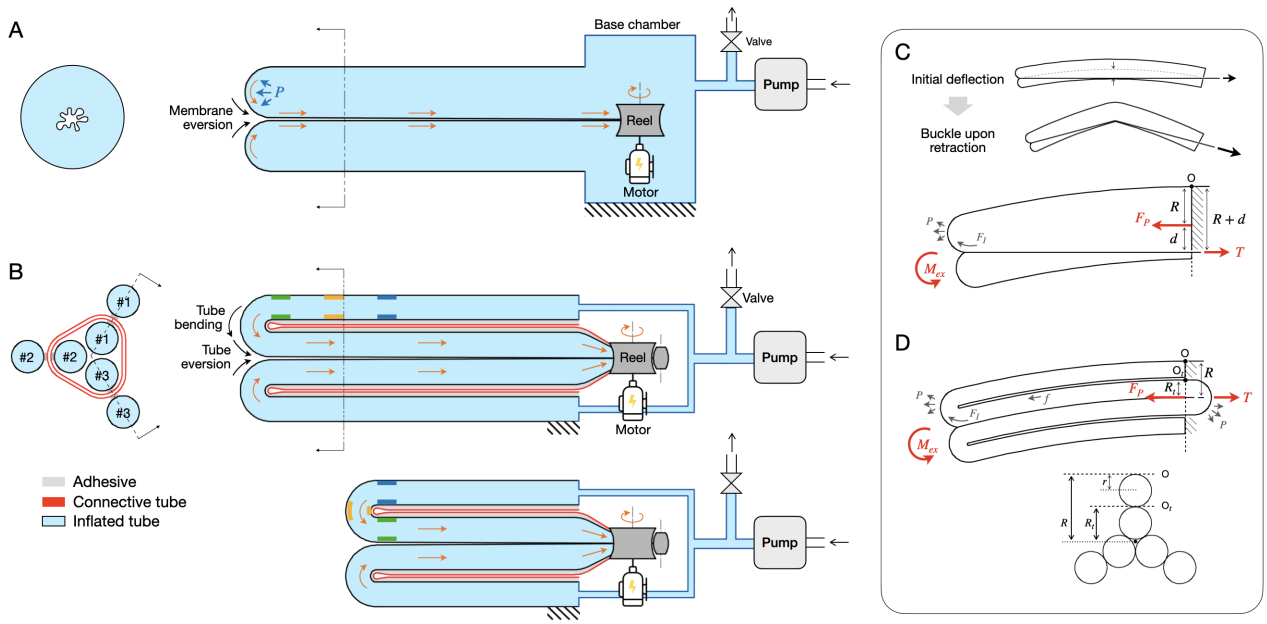


Fig. 2. Schematic sketch and analyses model of vine robot designs, (A) and (C) conventional design, (B) and (D) our design with bending-eversion

with $R$ and $R_t$ representing distances from the central line to points $O$ and $O_t$, respectively. The term $-T \cdot R_t$ arises because unlike the outer tubes that are longitudinally compressed by $T$, the tail is stretched by $T$ thus experiencing a straightening moment $T \cdot R_t$ (note that the tail rotates around the point $O_t$ during bending, this moment is therefore evaluated with respect to $O_t$). The definitions of $R$ and $R_t$ considering three inflated tubes are illustrated in Figure 2D.

The pressure-induced restoring moment $M_{restore}$ is evaluated as:

$$M_{restore} = \frac{1}{2} P \cdot A(R + R_t) \tag{8}$$

where $A$ denotes the total cross-sectional area of the robot, the terms $\frac{1}{2} P \cdot A \cdot R$ and $\frac{1}{2} P \cdot A \cdot R_t$ represents the moment associated with the outer tubes and the tails, evaluated with respect to point $O$ and $O_t$, respectively.

Then, the criterion for buckling-free retraction can be derived from Eq.(1):

$$\frac{1}{2} P \cdot A(R + R_t) \geq (F_I + f)(R - R_t) + M_{ex} \tag{9}$$

To compare the different retractability as predicted by Eq.(5) and Eq.(9), we calculate the maximum cantilevered length that allows buckling-free retraction using the two equations. The external moment from gravity under a cantilevered position can be calculated as:

$$M_{ex} = \frac{1}{2} \rho L^2 \tag{10}$$

with $\rho$ being the linear density of the robot along the length, and $L$ being the cantilevered length of the robot. For the calculation, we use the design parameters of our prototype robot (details in the next section), which has $\rho = 20$ g/m, and $A = 8.8$ cm$^2$. Testing determined $F_I$ to be approximately 4 N and $f$ to be 1 N per meter of the robot's length ($f = \lambda l$, where $\lambda = 1$ N/m and $l$ is the deployed length). Considering a conventional vine robot with the same total cross sectional area $A$ thus $R = 16.8$ mm, $\rho = 8$ g/m given by the same material thickness, and $F_I = 4$ N which is the same as our prototype and similar to literature [20]. The prediction results are plotted in Figure 3. It can be seen that the conventional robot can only achieve comparable cantilever retractability when $d = 0$, which is not possible as it requires the tail to be perfectly centered throughout the length. In reality, a conventional robot is likely to have $d = R$ due to the robot's curvature (as illustrated in Figure 2C).

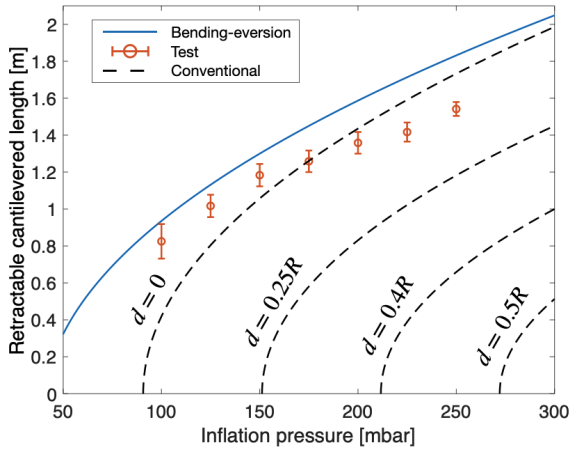


Fig. 3. Analyses and testing results for maximum cantilevered length with buckling-free retraction under various inflation pressures, dashed lines illustrate the behaviour of conventional vine robots with different amount of tail lateral shift, note that $d = R$ can be easily reached when the robot has an initial curvature, scale bar: standard deviation across 6 measurements

We have also experimentally measured the critical retractable cantilevered length of our prototype robot. Considering the 3-fold rotational symmetry of the robot's cross section, tests were conducted in all the three possible orientations that gives the cross sectional view illustrated in Figure 2D, and two measurements are taken from each orientation. During each measurement, the robot is retracted from a series of cantilevered length with a step of 5 cm, and the critical lengths for buckling-free retractions are reported in Figure 3. One possible cause of the mismatch between calculation and test is that higher cantilevered length tends to cause additional capstan friction due to the curvature of the cantilevered robot.

### C. Deployability Analysis

Unlike conventional vine robots, the deployment of bending vine robots is achieved by pushing the tail from the robot root, which is the reverse process of retraction. The maximum deployment force $D$, or the maximum axial growing force that the robot's tip can exert through elongation, is determined by the critical axial force that the tail can sustain. This force is not limited by longitudinal buckling since the tail is laterally constrained like a Bowden cable, but limited by collapsing. This means that the robot fails to deploy when the tail crashes along the axial direction as the pushing force overcomes the inflation pressure. The maximum pushing force therefore equals the inflation pressure force on the tail's cross section, $\frac{1}{2}P \cdot A$. When transmitted to the tip, this force is attenuated by the eversion force and the friction, becoming $\frac{1}{2}P \cdot A - F_I - f$. Recall that the robot's tip travels at half the speed of the tail, the maximum deployment force $D$ from our robot is thereby twice of the tail's pushing effect:

$$D = P \cdot A - 2F_I - 2f \tag{11}$$

The deployment force of our prototype is experimentally tested by deploying the robot with 0–0.5 m length against a load cell. Longer configurations are not tested since when a longer robot is axially compressed by a blocking force, it fails by overall longitudinal buckling that bends the entire robot including the tail and the outer tubes, which is similar to conventional vine robots and is beyond the scope of this study. The test result is plotted in Figure 4 with prediction from Eq.(11)

In comparison, conventional vine robots have a pressure driving force at the tip $P \cdot A$, and deployment also needs to overcome the everting force. The maximum deployment force of a conventional vine robot is thereby:

$$D = P \cdot A - 2F_I \tag{12}$$

According to Eq.(11) and Eq.(12), a vine robot with bending-eversion has similar deployability as a conventional one under nominal conditions, except in scenarios with magnified tail friction $f$, such as when the robot is radially compressed by an external force when passing through a narrow gap, or when the robot reaches a significant length. The effect of deployed length is predicted according to Eq.(11) and illustrated in Figure 4, using the previous approximation $f = \lambda l$, with $\lambda = 1$ N/m and $l$ being the deployed length.

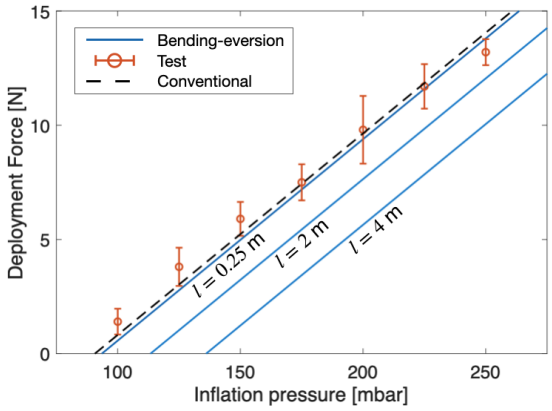


Fig. 4. Analyses and testing results for the deployment force under various inflation pressures, with conventional design (dashed line) and our design with various deployed length $l$ (solid lines), scale bar: standard deviation across 5 measurements

### D. Scalability Analysis

This section explores how retractable cantilevered length scales with cross sectional dimension of our design. We assume that the tube material has a constant thickness regardless of scaling. Therefore, the robot's linear density $\rho$ and the eversion force $F_I$ will scale linearly with the robot's cross-sectional perimeter, which is proportional to $R$, thus:

$$\rho \propto R \tag{13}$$

$$F_I \propto R \tag{14}$$

Then, according to Eq.(10), the scaling rule of external moment is as follows:

$$M_{ex} \propto R \cdot L^2 \tag{15}$$

Assuming that the retraction force $T$ (Eq.(6)) is dominated by everting force $F_I$, then according to Eq.(7) and Eq.(14), the bending moment caused by retraction scales as:

$$M_{retract} \propto R^2 \tag{16}$$

We assume the tube has constant thickness during scaling, and the robot operates near the bursting pressure for optimal performance. A tube with constant thickness has a bursting pressure proportional to its radius [23]. Therefore, scaling up requires a linear reduction of inflation pressure ($P \propto R^{-1}$). According to Eq.(8), the restoring moment scales as:

$$M_{restore} \propto R^2 \tag{17}$$

Now we can derive the scaling rule for buckling-free retraction from a cantilevered position with constant tube material thickness and near bursting pressure using Eq.(1), which gives:

$$\frac{L^2}{R} \approx \text{constant} \tag{18}$$

This indicates that the ratio $L^2 \cdot R^{-1}$ is approximately independent of scaling, i.e., a robot with a larger cross-sectional radius can allow a longer retractable cantilevered length under a certain tube material thickness. In the test result reported in Figure 3, the prototype robot has achieved $L^2 \cdot R^{-1} > 50$ m.

## III. IMPLEMENTATION

In this section, we present the design and fabrication of the main components of a vine robot with bending-induced eversion: soft everting body, retraction mechanism, and inflation system. The total mass of our demonstration prototype is 930 g. Table I provides a breakdown of the system's mass distribution.

TABLE I
DEMONSTRATOR ROBOT MASS BREAKDOWN

| Component | Mass (g) |
|---|---|
| Soft everting body (2 m) | 40 |
| Retraction Mechanism | 435 |
| Inflation & control system | 455 |
| **Total** | **930** |

### A. Soft Everting Body

The everting body uses heat-welded polyethylene (PE) tubes with a thickness of 50 m. The inflated tubes and the connective tube have circumferences of 40 mm and 100 mm, respectively. The inflated tubes are bonded onto the connective tube using 3M 9080 tape with a thickness of 160 m, a double-sided pressure sensitive acrylic adhesive tape with a paper carrier. The finished robot body has a density of 20 g per meter length of the robot.

### B. Retraction Mechanism

Although no deploying force or retraction resistance is experienced by the robot's tip, substantial force is needed to deflate and retract the tubes onto the mandrel. Such forces are localised at the retraction reel, having no impact on the robot's stability. Retraction requires a motor-generated torque to counteract the inflation pressure that tends to unreel the tail from the mandrel, and a compression force to prevent the tail from inflating on the mandrel. A retraction reel is therefore designed to provide both the retraction torque and mechanical deflation pressure, as depicted in Figure 5A.

The retraction reel system consists of a belt that compresses onto the mandrel when the belt pulleys are tensioned by a spring. One pulley is installed on the frame and driven by the motor, while the other pulleys and the mandrel are free to rotate and move in the plane of rotation. During retraction, the belt compresses the tail against the mandrel to deflate it, while transmitting the motor torque to rotate the mandrel. The compliance of the belt allows the mandrel and pulleys to adapt to the increasing thickness of the retracted material on the mandrel, maintaining consistent compression force.

The pressing effect exerted by the belt on the mandrel can be calculated according to Figure 5B using the simple capstan equation [27]:

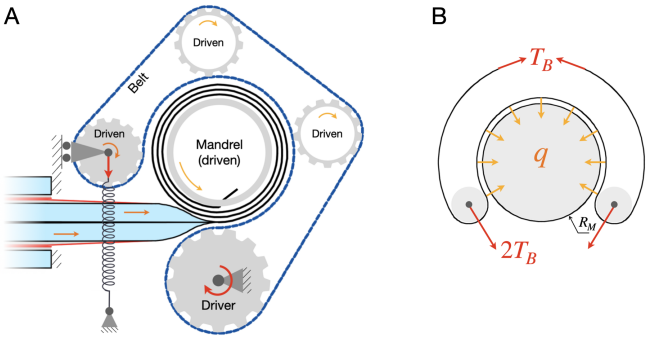


Fig. 5. The belt-driven retraction mechanism, (A) schematic sketch, (B) simplified model for analyses

$$q = \frac{T_B}{R_M} \tag{19}$$

where $q$ is the distributed load (in N/m) on the mandrel of radius $R_M$ resulting from belt tension $T_B$. Successful retraction requires that the mechanical compression (characterised by $q/D$, with $D = 0.05$ m being the mandrel's width) exceeds the inflation pressure $P$. If the inflation pressure overcomes this compression, the tail inflates on the mandrel, causing retraction failure. We validated this design by testing with various springs with differing tensions, and measured the critical inflation pressure at which the tail begins to inflate on the mandrel. The result is plotted in Figure 6, along with predictions from Eq.(19).

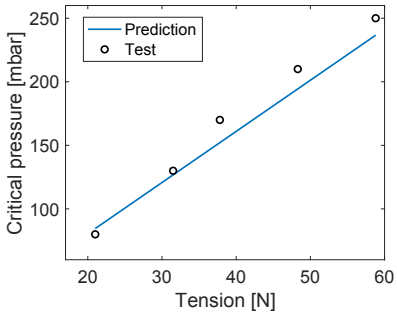


Fig. 6. Critical inflation pressure at which the tail begins to inflate on the retraction mandrel, under various spring tensions

Figure 7 illustrates the implementation of the retraction reel mechanism in our prototype. The belt is a Megadyne Megapower T10 timing belt made from TPU material. A geared DC brushed motor directly drives a 18-tooth pulley. The geared motor has a reduction ratio of 260, a rated output torque of 1 N·m, a rated power of 3.6 W, and a mass of 160 g. The pulleys and structural components are fabricated using 3D printed ABS. Metallic springs are used to apply tension. This system allows for a retraction speed of approximately 4 cm/s, and a robot with 2 m total length can be successfully retracted.

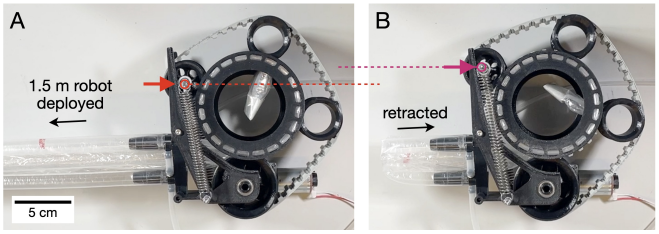


Fig. 7. The retraction mechanism, with belt geometry adapting to varying thickness of retracted material, from (A) the deployed state to (B) the retracted state

### C. Inflation and Control System

The robot is inflated using a diaphragm pump, which has a rated power of 20 W, and a mass of 300 g. Inflation pressure is regulated using a solenoid valve controlled by an Arduino nano board and an Adafruit MPRLS pressure sensor. The valve weighs 90 g. During operation, the pump runs continuously at full voltage while the valve switches on/off to modulate pressure. This system can achieve maximum and minimum inflation pressures of 250 mbar and 100 mbar during deployment and retraction at the speed of 4 cm/s.

## IV. DEMONSTRATIONS

Eversion through bending enables new designs and functionalities that are not possible in conventional vine robots. A demo of these designs is visible in the video accompanying the article.

Figure 8 shows an eversion-based robotic gripper, which uses the same vine robot tested earlier with no modifications. Thanks to its retractable multi-tube body, the robot transports external objects along its length during retraction, while the soft body conforms to the shape of the target for grasping. It is interesting to note that the robot creates a ”buffer” zone for storing objects, allowing for continuous gripping before switching to releasing mode (i.e., deploying mode). In applications like fruit harvesting, this can reduced the gripper’s downtime.

The size of graspable objects is limited by friction, as larger objects cause higher pressing force between the tail and the outer tube, leading to excessive friction and the robot can fail to release the object (i.e., the tail crushes near the root during deployment as discussed in Section II-C). Similarly, friction also increases with the number of objects simultaneously buffered in the robot body, limiting the number of object that can be collected and stored inside the body. We have experimentally measured the maximum number of objects that can be grasped, simultaneously buffered and released from the vine robot, as reported in Figure 8. During the tests, spherical and cubic objects with different sizes manufactured by resin 3D printing were placed on a flat bench, and the vine robot approached vertically from above. The robot was unable to pickup cubic objects with side length below 8 mm, or spheres with diameter below 12 mm, where the cubic objects are easier to grasp as they have higher diagonal length. For the graspable objects, the robot was loaded until it failed to release the objects due to friction-induced deployment failure, and the result shows that larger objects reduce the buffer capacity, while the maximum releasable sizes are 16 mm and 18 mm for cubic and spherical objects, respectively.

Utilising the capability to operate under a cantilevered position, we demonstrated its application as a deployable arm onboard a drone. The vine robot was installed under a DJI Matrice 300 RTK drone platform, at a 30° downward angle to avoid the risk of propeller impacts, as shown in Figure 9. We used this setup to demonstrate a potential application in environmental DNA (eDNA) sampling, which usually relies on manual collection methods [28], and robotic collections are usually limited to the outermost tree canopies [29]. By deploying the vine robot into tree canopies, we provide a potential opportunity to interact with the inner branches and thereby collect the localised eDNA samples. Adhesive materials reported in our previous study can be implemented on the vine robot outer surface to enhance sample acquisition [29], which will not affect the deployment and retraction since the outer surface is everted into the center of the tail, causing no advert friction.

Eversion through bending also enables solid-state vine robots that do not require inflation. Figure 10 presents a vine robot composed of soft foam material, which consists of three foam rods bonded through one connective tube. The design and fabrication methods are similar to the vine robot demonstrated above. Removal of inflation can simplify the system, potentially allowing lower-power, lightweight robots with enhanced environmental robustness (e.g., against punctures, heat, etc.). This approach, however, comes with the trade-off of less compact storage of the retracted material compared to inflatable designs.

## V. CONCLUSIONS

We have created a new type of vine robots comprising multiple interconnected tubes that evert through bending. This eversion method leads to a simplified design without tip-mounted device or pressurised base chamber, whilst enabling buckle-free retraction even under cantilevered position. A demonstrator robot is designed and fabricated. Tests have verified its retractable cantilevered length of over 1 m under an inflation pressure above 100 mbar, as well as a deployment/growing force comparable to conventional vine robots. The robot has also demonstrated its function as a robot gripper with an internal buffer to store objects, as well as a deployable cantilevered arm onboard a drone platform.

This unique multi-tube design also leads to limitations. Compared to conventional vine robots with tip-devices, our design is more sensitive to capstan friction, which limits the applications that require the robot to be extensively curved. In our robot, the friction force between the inflated tail and the inflated outer tubes is approximately 1 N per meter of robot length, which is similar to conventional vine robots [30]. However, when navigating curved paths, friction increases due to capstan effect that depends on the tension in the tail [27]. For a conventional vine robot with tip-device,

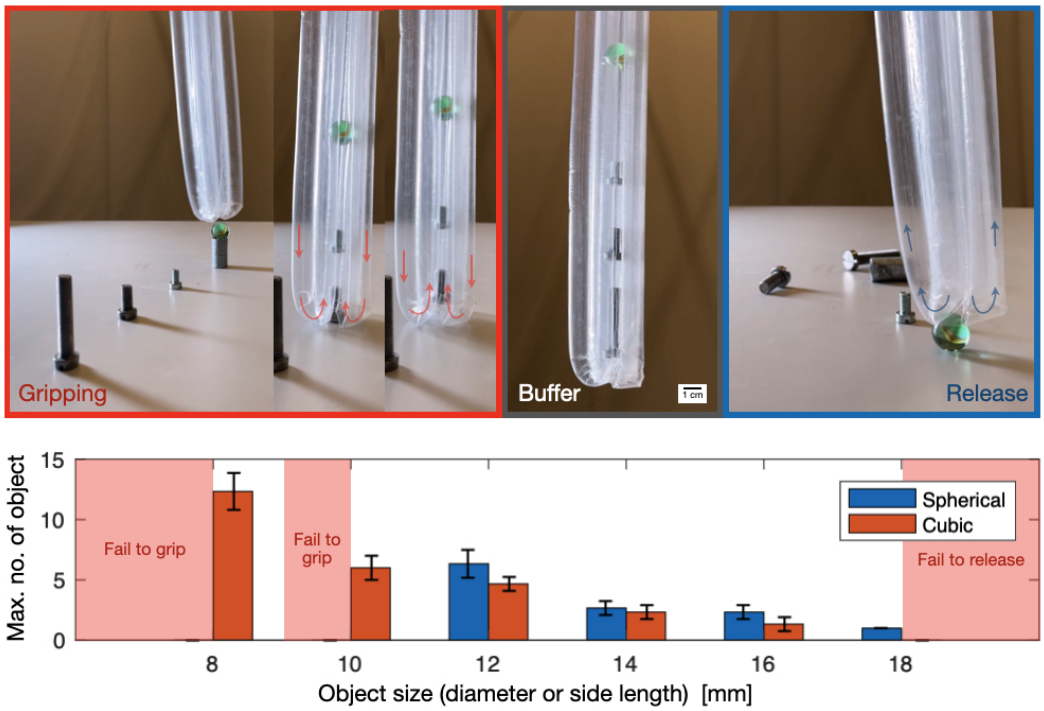


Fig. 8. Everting soft gripper with a "buffer" zone that allows continuous grasping of objects with various shapes (top), test result on the maximum number of objects to be grasped and buffered, with different object sizes and shapes, scale bar: standard deviation from three tests (bottom)


Fig. 9. Drone-based cantilevered vine robot with potential applications in environmental DNA (eDNA) sampling from inner tree canopies, demonstrated by deployment into a pine tree (Pinus peuce) (left) and a cypress tree (Sequoioideae) (lower right), the demonstration system (upper right)


Fig. 10. Solid-state vine robot comprised of foam robds everting through bending, which removes the need for inflation

the tension during deployment is only caused by friction between the tail and the deployed body, whilst in our design, the everting force also contributes to this tension. Consequently, our design experiences higher capstan friction, which leads to a higher tendency of jamming during deployment when the robot takes a curved path. Meanwhile, external radial load can also cause excessive friction in our robot. When the robot is pinched, the tail will press against the outer tube, leading to friction-induced jamming. This limitation prevents the robot from performing applications that require passages through narrow gaps, and as mentioned earlier, the buffer capacity of everting grippers. As a future prospect, low-friction or lubricating materials can be exploited to reduce the friction-induced issues discussed above, and enable a larger operation envelop.

We anticipate that our vine robot that everts through bending will open new opportunities for future growing robots with innovative functionalities, expanded operation scenarios, and simplified designs.

## REFERENCES


[1] E. W. Hawkes, L. H. Blumenschein, J. D. Greer, and A. M. Okamura, "A soft robot that navigates its environment through growth," *Science Robotics*, vol. 2, no. 8, p. eaan3028, 2017.

[2] L. H. Blumenschein, M. M. Coad, D. A. Haggerty, A. M. Okamura, and E. W. Hawkes, "Design, modeling, control, and application of everting vine robots," *Frontiers in Robotics and AI*, vol. 7, p. 548266, 2020.

[3] P. A. Der Maur, B. Djambazi, Y. Haberthür, P. Hörmann, A. Kübler, M. Lustenberger, S. Sigrist, O. Vigen, J. Förster, F. Achermann, *et al.*, "Roboa: Construction and evaluation of a steerable vine robot for search and rescue applications," in *2021 IEEE 4th International Conference on Soft Robotics (RoboSoft)*. IEEE, 2021, pp. 15–20.

[4] M. M. Coad, L. H. Blumenschein, S. Cutler, J. A. R. Zepeda, N. D. Naclerio, H. El-Hussieny, U. Mehmood, J.-H. Ryu, E. W. Hawkes, and A. M. Okamura, "Vine robots," *IEEE Robotics & Automation Magazine*, vol. 27, no. 3, pp. 120–132, 2019.

[5] J. Luong, P. Glick, A. Ong, M. S. DeVries, S. Sandin, E. W. Hawkes, and M. T. Tolley, "Eversion and retraction of a soft robot towards the exploration of coral reefs," in *2019 2nd IEEE International Conference on Soft Robotics (RoboSoft)*. IEEE, 2019, pp. 801–807.

[6] J. D. Greer, T. K. Morimoto, A. M. Okamura, and E. W. Hawkes, "A soft, steerable continuum robot that grows via tip extension," *Soft robotics*, vol. 6, no. 1, pp. 95–108, 2019.

[7] A. M. Gruebele, A. C. Zerbe, M. M. Coad, A. M. Okamura, and M. R. Cutkosky, "Distributed sensor networks deployed using soft growing robots," in *2021 IEEE 4th International Conference on Soft Robotics (RoboSoft)*. IEEE, 2021, pp. 66–73.

[8] P. Slade, A. Gruebele, Z. Hammond, M. Raitor, A. M. Okamura, and E. W. Hawkes, "Design of a soft catheter for low-force and constrained surgery," in *2017 IEEE/RSJ International Conference on Intelligent Robots and Systems (IROS)*. IEEE, 2017, pp. 174–180.

[9] M. Li, R. Obregon, J. J. Heit, A. Norbash, E. W. Hawkes, and T. K. Morimoto, "Vine catheter for endovascular surgery," *IEEE Transactions on Medical Robotics and Bionics*, vol. 3, no. 2, pp. 384–391, 2021.

[10] T. Nakamura and H. Tsukagoshi, "Soft pneumatic manipulator capable of sliding under the human body and its application to preventing bedsores," in *2018 IEEE/ASME International Conference on Advanced Intelligent Mechatronics (AIM)*. IEEE, 2018, pp. 956–961.

[11] S. Wang, R. Zhang, D. A. Haggerty, N. D. Naclerio, and E. W. Hawkes, "A dexterous tip-extending robot with variable-length shape-locking," in *2020 IEEE International Conference on Robotics and Automation (ICRA)*. IEEE, 2020, pp. 9035–9041.

[12] S. E. Root, D. J. Preston, G. O. Feifke, H. Wallace, R. M. Alcoran, M. P. Nemitz, J. A. Tracz, and G. M. Whitesides, "Bio-inspired design of soft mechanisms using a toroidal hydrostat," *Cell Reports Physical Science*, vol. 2, no. 9, 2021.

[13] N. D. Naclerio, C. M. Hubicki, Y. O. Aydin, D. I. Goldman, and E. W. Hawkes, "Soft robotic burrowing device with tip-extension and granular fluidization," in *2018 IEEE/RSJ International Conference on Intelligent Robots and Systems (IROS)*. IEEE, 2018, pp. 5918–5923.

[14] N. D. Naclerio, A. Karsai, M. Murray-Cooper, Y. Ozkan-Aydin, E. Aydin, D. I. Goldman, and E. W. Hawkes, "Controlling subterranean forces enables a fast, steerable, burrowing soft robot," *Science Robotics*, vol. 6, no. 55, p. eabe2922, 2021.

[15] K. Eken, N. Gravish, and M. T. Tolley, "Continuous skin eversion enables an untethered soft robot to burrow in granular media," in *2023 IEEE International Conference on Soft Robotics (RoboSoft)*. IEEE, 2023, pp. 1–6.

[16] N. Agharese, T. Cloyd, L. H. Blumenschein, M. Raitor, E. W. Hawkes, H. Culbertson, and A. M. Okamura, "Hapwrap: Soft growing wearable haptic device," in *2018 IEEE International Conference on Robotics and Automation (ICRA)*. IEEE, 2018, pp. 5466–5472.

[17] Y. Satake, A. Takanishi, and H. Ishii, "Novel growing robot with inflatable structure and heat-welding rotation mechanism," *IEEE/ASME Transactions on Mechatronics*, vol. 25, no. 4, pp. 1869–1877, 2020.

[18] L. H. Blumenschein, M. Koehler, N. S. Usevitch, E. W. Hawkes, D. C. Rucker, and A. M. Okamura, "Geometric solutions for general actuator routing on inflated-beam soft growing robots," *IEEE Transactions on Robotics*, vol. 38, no. 3, pp. 1820–1840, 2021.

[19] P. E. Glick, I. Adibnazari, D. Drotman, D. Ruffatto III, and M. T. Tolley, "Branching vine robots for unmapped environments," *Frontiers in Robotics and AI*, vol. 9, p. 838913, 2022.

[20] M. M. Coad, R. P. Thomasson, L. H. Blumenschein, N. S. Usevitch, E. W. Hawkes, and A. M. Okamura, "Retraction of soft growing robots without buckling," *IEEE Robotics and Automation Letters*, vol. 5, no. 2, pp. 2115–2122, 2020.

[21] L. H. Blumenschein, N. S. Usevitch, B. H. Do, E. W. Hawkes, and A. M. Okamura, "Helical actuation on a soft inflated robot body," in *2018 IEEE International Conference on Soft Robotics (RoboSoft)*. IEEE, 2018, pp. 245–252.

[22] H. Dehghani, C. R. Welch, A. Pourghodrat, C. A. Nelson, D. Oleynikov, P. Dasgupta, and B. S. Terry, "Design and preliminary evaluation of a self-steering, pneumatically driven colonoscopy robot," *Journal of medical engineering & technology*, vol. 41, no. 3, pp. 223–236, 2017.

[23] W. E. Heap, N. D. Naclerio, M. M. Coad, S.-G. Jeong, and E. W. Hawkes, "Soft retraction device and internal camera mount for everting vine robots," in *2021 IEEE/RSJ International Conference on Intelligent Robots and Systems (IROS)*. IEEE, 2021, pp. 4982–4988.

[24] T. Takahashi, M. Watanabe, K. Tadakuma, M. Konyo, and S. Tadokoro, "Retraction mechanism of soft torus robot with a hydrostatic skeleton," *IEEE Robotics and Automation Letters*, vol. 5, no. 4, pp. 6900–6907, 2020.

[25] N. G. Kim and J.-H. Ryu, "A soft growing robot using hyperelastic material," *Advanced Intelligent Systems*, vol. 5, no. 2, p. 2200264, 2023.

[26] U. Jeong and K.-J. Cho, "A feasibility study on tension control of bowden-cable based on a dual-wire scheme," in *2017 IEEE international conference on robotics and automation (ICRA)*. IEEE, 2017, pp. 3690–3695.

[27] M. Kaneko, T. Yamashita, and K. Tanie, "Basic considerations on transmission characteristics for tendon drive robots," in *Fifth International Conference on Advanced Robotics' Robots in Unstructured Environments*. IEEE, 1991, pp. 827–832.

[28] R. E. Valentin, D. M. Fonseca, S. Gable, K. E. Kyle, G. C. Hamilton, A. L. Nielsen, and J. L. Lockwood, "Moving edna surveys onto land: Strategies for active edna aggregation to detect invasive forest insects," *Molecular Ecology Resources*, vol. 20, no. 3, pp. 746–755, 2020.

[29] E. Aucone, S. Kirchgeorg, A. Valentini, L. Pellissier, K. Deiner, and S. Mintchev, "Drone-assisted collection of environmental dna from tree branches for biodiversity monitoring," *Science Robotics*, vol. 8, no. 74, p. eadd5762, 2023.

[30] L. H. Blumenschein, A. M. Okamura, and E. W. Hawkes, "Modeling of bioinspired apical extension in a soft robot," in *Conference on Biomimetic and Biohybrid Systems*. Springer, 2017, pp. 522–531.